Applied Catalysis B: Environmental 262 (2020) 118246

Contents lists available at ScienceDirect

Applied Catalysis B: Environmental

journal homepage: www.elsevier.com/locate/apcatb

Enhanced catalyst dispersion and structural control of Co_3O_4-silica nanocomposites by rapid thermal processing

Liang Liu[a,*], Jia Ding[b], Gholamreza Vahedi Sarrigani[b], Paul Fitzgerald[c], Zulkifli Merican Aljunid Merican[d], Jun-Wei Lim[e], Hui-Hsin Tseng[f], Fengwei Xie[g,h], Binjia Zhang[i], David K. Wang[b,*]

[a] School of Chemical Engineering, The University of Melbourne, Victoria, 3010, Australia
[b] School of Chemical and Biomolecular Engineering, The University of Sydney, New South Wales, 2006, Australia
[c] Sydney Analytical, Core Research Facilities, The University of Sydney, New South Wales, 2006, Australia
[d] Department of Fundamental and Applied Sciences, Universiti Teknologi PETRONAS, 32610 Seri Iskandar, Perak Darul Ridzuan, Malaysia
[e] Department of Fundamental and Applied Sciences, Centre for Biofuel and Biochemical Research, Institute of Self-Sustainable Building, Universiti Teknologi PETRONAS, 32610 Seri Iskandar, Perak Darul Ridzuan, Malaysia
[f] School of Occupational Safety and Health, Chung Shan Medical University, Taichung, 402, Taiwan, ROC
[g] International Institute for Nanocomposites Manufacturing (IINM), WMG, University of Warwick, Coventry, CV4 7AL, United Kingdom
[h] School of Chemical Engineering, The University of Queensland, Brisbane, Qld, 4072, Australia
[i] Key Laboratory of Environment Correlative Dietology, College of Food Science and Technology, Huazhong Agricultural University, Wuhan, 430070, China

ARTICLE INFO

Keywords:
Sol-gel
Rapid thermal processing
Cobalt tetroxide silica
Fenton reaction
Heterogeneous catalysis

ABSTRACT

We synthesized cobalt tetroxide (Co_3O_4) silica nanocomposites based on the conventional tetraethyl orthosilicate (TEOS) monomer and ethoxy polysiloxane (ES40) oligomer by sol-gel chemistry coupled with rapid thermal process (RTP). The physicochemical properties and structural formation of cobalt oxide silica nanocomposites were comprehensive characterized. By using ES40, well-controlled, homogeneous nanoparticle dispersion and size of Co_3O_4 with 5 nm within the silica matrix were achieved leading to fractal-like morphology. The concentration of the Co_3O_4 nanocatalyst was also significantly enhanced by more than 50 folds. Fenton-like HCO_3^-/H_2O_2 catalytic system using acid orange 7 and nanocomposites was examined for organic degradation. 98% AO7 and naphthalene intermediates degradation efficiency was achieved after 20 min with ES40-derived catalyst, which was three to ten folds faster than that of the TEOS-derived catalyst and the commercial Co_3O_4 catalyst. The combined use of ES40 sol-gel and RTP enabled a simple way to nanomaterial preparation and lowers overall processing time.

1. Introduction

Cobalt and cobalt oxide containing nanomaterials are of great interest in many advanced technological applications, such as membrane separation [1], catalysis [2,3], electrochemical [4], and gas-sensing devices [5–8]. For examples, metallic cobalt is an important catalyst for Fischer-Tropsch processing and it is normally reduced from cobalt oxides [9], and cobalt tetroxide (Co_3O_4) nanoparticles are promising catalyst candidates for water splitting [2,10], toxic gas treatment [11,12], and degradation of organic pollutants [13,14] due to their high catalytic activity, stability and abundance. Another example shows that nano-scale Co_3O_4 demonstrated better catalytic activity and selectivity than the bulk counterpart due to a high surface-volume ratio, morphology-dependent properties and high concentration of active sites [14]. Lin et. al. investigated the effects of the microstructure of Co_3O_4 supported in porous silica nanocomposites on the water oxidation activity and found that porous silica shells of up to ~20 nm in thickness led to the increased water oxidation activity [15]. Moreover, Chou et. al. showed that nanostructural control of Co_3O_4, CoO, and ε-Co catalyst with similar size, shapes and surface stabilizers exhibited very similar water oxidation activities under basic conditions [16]. Thus, the catalytic performance of the Co_3O_4 nanoparticles is critically dependent on the morphology, physicochemical properties and dispersion of cobalt oxide species on the support, which can be controlled by synthesis conditions, choice of support, and post-treatments.

A significant body of the literature on cobalt-containing nanomaterials has been found using sol-gel process, which is a versatile, simple method to synthesize silica-supported Co_3O_4 catalysts as it provides

* Corresponding authors.
E-mail addresses: liang.liu@unimelb.edu.au (L. Liu), david.wang1@sydney.edu.au (D.K. Wang).

https://doi.org/10.1016/j.apcatb.2019.118246
Received 18 June 2019; Received in revised form 24 September 2019; Accepted 28 September 2019
Available online 12 October 2019

excellent control of physicochemical properties of the nanomaterials. For examples, recent studies on cobalt oxide silica membranes derived from sol-gel method showed excellent separation performance for H_2/CO_2 separation [1] and water desalination [17]. The incorporation of cobalt oxide nanoparticles in silica matrix also confers improved stability of the silica matrix, which enabled these membranes to be operated under aggressive conditions. Moreover, we have previously reported that the formation of Co_3O_4 in the silica matrix could be tuned by varying cobalt concentration [18] and sol-gel conditions (e.g. the ratio of water and ethanol in the solution) to improve material stability and morphological properties for high-temperature gas separation [19]. These studies led to the discovery of the important role of Co_3O_4 in the silica matrix to enable membrane hydrothermal stability as Co_3O_4 was found to prevent water attack on the energetic silica surface due to the presence of long-range order interaction with the silica [20]. Nevertheless, the sol-gel preparation process involves a slow heating/cooling post-treatment step, which can last for 20 h and thus is very time-consuming and energy-intensive [21,22]. If production time and energy can be reduced, then it is commercially attractive to develop a more efficient, post-treatment method to minimise the economic penalties associated with fabrication.

Here, we report a rapid thermal processing (RTP) treatment and sol-gel chemistry to prepare highly-dispersed, nano-sized, cobalt oxide silica materials using two different types of silica precursors, i.e. tetraethyl orthosilicate (TEOS) and ethoxy polysiloxane (ES40), which exhibited excellent structure-property-performance relationship for the treatment of organic hazardous dye compound. Furthermore, we comprehensively studied the effect of RTP and precursor structure under in-situ, synchrotron small-angle X-ray scattering to fully elucidate the mechanism behind structural formation of the Co_3O_4-silica catalyst during rapid heat processing.

2. Experimental

2.1. Materials

Cobalt oxide silica materials were prepared by a modified sol-gel method [23]. Briefly, cobalt nitrate hexahydrate ($Co(NO_3)_2{\cdot}6H_2O$, 98%, Sigma-Aldrich) was dissolved in a mixture of double distilled water, ethanol (99%, AR grade) and nitric acid (HNO_3; 70% AR grade, RCI Labscan). Then, tetraethyl orthosilicate (TEOS; Sigma Aldrich) or ethyl silicate 40 (ES40; Colcoat Co., Japan) was added drop-wisely in the mixture and the specific molar compositions of TEOS or ES40 : Co $(NO_3)_2{\cdot}6H_2O$: EtOH : H_2O : HNO_3 were 4 :1 : 255 : 46 : 0.01. Both solutions were stirred for 10 min at room temperature, and then they were dropped on Petri dishes and dried in an oven at 80 °C for 30 min. The dried samples were directly calcined in a pre-heated furnace at 600 °C for 1 h.

2.2. Material characterizations

Nitrogen sorption measurements were carried out on a Micromeritics Tristar 3000 analyzer. Both samples were degassed at 200 °C on a Micromeritics VacPre061 for a minimum of 6 h before the measurement. The Brunner-Emmett-Teller (BET) method was used to calculate the specific surface area. Pore size distribution was analyzed using built-in density functional theory (DFT) in the Micromeritics analyzer software on the adsorption isotherms. Cylindrical pores in an oxide surface with a low regularization was chosen to represent our materials.

Fourier transform infrared-attenuated total reflectance (FTIR-ATR) spectra were collected from a Shimadzu IRAffinity-1 with an ATR attachment. Spectra were taken over a wavenumber range of 4000–500 cm^{-1} with a resolution of 4 cm^{-1}. Peak fitting was performed with the Fityk software (version 0.9.4) with Gaussian peak shapes. The peak position and height were allowed to vary to achieve the best fit.

X-ray photoelectron spectroscopy (XPS) spectra were collected from a Kratos Axis ULTRA XPS with a 165 mm hemispherical electron energy analyser. Al-Kα X-rays (1486.6 eV) were used as the incident radiation at 45° to the sample surface with a monochromator. 250 ms dwell time and 0.1 eV steps at pass energy of 20 eV were set for the high-resolution scan of Co 2p spectra. CasaXPS software (Version 2.3.14) was used for curve fitting. Adventitious carbon at 284.6 eV was used as a reference to calibrate the spectra.

X-ray diffraction (XRD) data were collected on a Bruker D8 Advance with a graphite monochromator using Cu-Kα over 20–100° 2θ at an operating voltage of 40 kV and amperage of 40 mA with a scanning rate of 3.2 s/step. The long-time accumulation scans collected between 32–43° 2θ used a scanning rate of 30 s/step.

X-ray absorption spectroscopy data at the Co K-edge (E_0 = 7709 eV) was collected at the wiggler XAS Beamline at the Australian Synchrotron. The energy axis was calibrated using a cobalt metal foil. The energy grid was stepped at 0.3 eV closing to the absorption edge, and constant steps in k-space (Δk = 0.035 $Å^{-1}$) was used for the data in the EXAFS (Extended X-ray Absorption Fine Structure) region. Spectra of CoO and Co_3O_4 were recorded as reference materials to assist with data interpretation. The freeware VIPER [24] was used to analyze EXAFS data as reported in a previous study [20].

For synchrotron small- and wide-angle X-ray scattering (SAXS/WAXS) measurements, the hydrated sol-gel samples after the initial 10 min mixing were placed in capillary quartz tubes (Hilgenberg, Germany) of 80 mm length, 1.5 mm diameter with a ~10 µm wall thickness. SAXS/WAXS measurements with 1 s acquisition were carried out on the SAXS/WAXS beamline (flux, 10^{13} photons/s) installed at the Australian Synchrotron (Clayton, Australia), at a wavelength λ = 1.13 Å. The in-situ heating (100 °C min^{-1}) was carried out using a hot-stage with a Serpentine Air heater system, and the 2D scattering patterns were recorded using a Pilatus 1 M camera (active area 169 × 179 mm and pixel size 172 × 172 µm) every 10 s. Using the scatterBrain software, 1D data were reduced from the 2D scattering patterns in the angular range of $0.01 < q < 0.4\ Å^{-1}$, in which $q = 4\pi\sin\theta/\lambda$ (where 2θ is the scattering angle and λ is the wavelength of the X-ray source). All data were corrected for transmission, empty capillary scattering background subtracted and normalized to the direct beam intensity. Data was fit in the SASView fitting package [25] using the sphere [26], and mass fractal models [27].

Transmission electron microscopy (TEM) images were obtained on a JEOL 1010 electron microscope with an acceleration voltage of 100 kV.

2.3. Acid orange 7 degradation experiment

AO7 ($C_{16}H_{11}N_2NaO_4S$, M_w: 350.32 g mol^{-1}, Sigma-Aldrich) was chosen as a model pollutant to investigate the catalytic activity of the cobalt oxide silica samples. All experiments were performed using a desired amount of sample (0.2 g L^{-1}) and $NaHCO_3$ (3.6 mM) in AO7 (50 ppm, 0.14 mM) aqueous solution of 250 mL at room temperature [3,28]. The solution was stirred for 0.5 h to reach adsorption equilibrium in dark condition. The reactions were then initiated by adding H_2O_2 (11 mM) into the suspension. Samples were periodically withdrawn, filtered through 0.2 µm Millipore syringe filters and immediately analysed. The AO7 degradation as a function of reaction time was analysed by measuring the absorbance of the solution at λ_{max} = 484 nm using a UV–vis spectrophotometer (Evolution 220, ThermoFisher Scientific).

3. Results and discussion

3.1. Physicochemical properties

Chemical properties of the Co_3O_4-silica catalysts are shown in Fig. 1a–c by FTIR-ATR and XPS spectroscopies. Fig. 1a shows

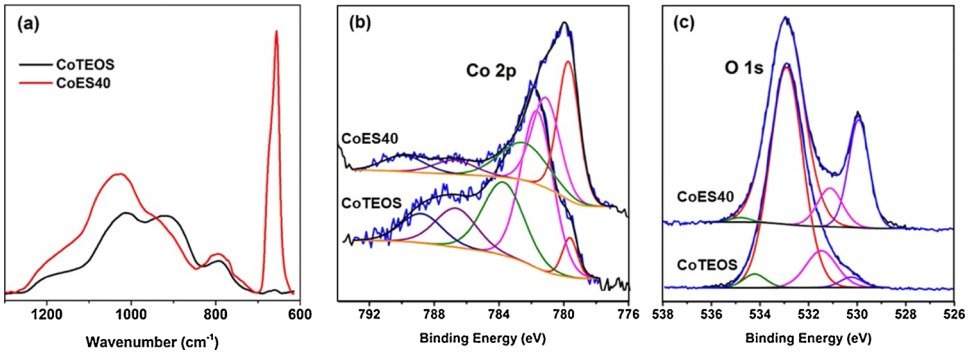

Fig. 1. (a) FTIR-ATR spectra and high-resolution XPS spectra of (b) Co 2p ($2p_{3/2}$ component) and (c) O 1s for the CoTEOS and CoES40 samples.

characteristic siloxane bonds with bands near 800, 1030, 1090 and 1160 cm^{-1} and silanol bonds at 930 cm^{-1} as well as an intense strong cobalt tetroxides (Co_3O_4) peak near 670 cm^{-1} for CoES40 sample, despite only a very weak vibration of the latter band could be detected for the CoTEOS. The most intense peak at 1030 cm^{-1} was used as normalization because it was determined as the most stable and least varying peak in both CoTEOS and CoES40 spectra. Fig. S1a and b (ESI†) show significant changes occurring in these regions especially a peak reduction of 930 cm^{-1} of the silanol groups was compensated by an enhanced siloxane vibrations in the range between 1100–1250 cm^{-1} in CoES40. Notably, area ratio of the Co_3O_4 peaks within 672 cm^{-1} to 639 cm^{-1} region shows that the relative concentration of Co_3O_4 catalyst in CoES40 was 50 folds greater than that of the CoTEOS as shown in Fig. S1b (ESI†).

Fig. 1b and c display the XPS analysis, which further confirm the presence of cobalt species. High-resolution XPS spectra of Co 2*p* and O 1*s* of the synthesized catalysts are compared. In the Co 2*p* spectra of the cobalt species as shown in Fig. 1b, both the $2p_{1/2}$ and $2p_{3/2}$ components due to spin-orbit splitting are present but only the higher-intensity $2p_{3/2}$ bands were curve-fitted, including the shake-up satellites of the cobalt (II) ions. The two main peaks near 779.6 eV and 781 eV are assigned to Co(III) and Co(II) oxidation states of the cobalt oxide species respectively, which can be clearly observed in all the samples. The intensity of the former peak for the Co(III) ions characteristic of the Co_3O_4 species increases in the order for the CoTEOS and CoES40 samples, which is evidenced by the absence of the shake-up satellites can be observed near 787 eV in CoES40 [29]. This band shows an increased proportion in the CoTEOS sample, indicating that the cobalt oxides are mainly in the 2+ oxidation state as the Co(III) oxides do not have shake-up satellites. Additionally, the O 1s peak at 529.8 eV (Fig. 1c) assigned to the oxide ions of the Co_3O_4 [30] also grows in concert with the intensity of the band at 779.6 eV for the Co_3O_4. It is important to mention that the presence of the Co metal peak occurring in the lower BE region at 778.1 eV [31] was not observed in both samples.

3.2. Co_3O_4 nanoparticle morphological structure

Phase analysis confirmed a secondary cobalt phase in the amorphous silica matrix, indexed to spinel Co_3O_4 (JCPDS 42–1467, Fig. 2a) with diffraction lines registered at 2θ value of 36.9°, 44.9°, 55.7°, 59.5° and 65.4°, which correspond to the crystal planes (311), (400), (422), (511) and (440) respectively. Close examination of the (311) reflection over the 34–40° 2*θ* region as shown by the inset image indicated crystalline Co_3O_4 was present in both samples. Average crystallite sizes for Co_3O_4 in CoTEOS and CoES40 were calculated as 44 and 14 nm respectively using Scherrer's equation.

Fig. 2b and c show the TEM images of the nanocomposites of CoTEOS and CoES40, respectively. Firstly, there is no discernible difference in the silica phase and both show homogenous, amorphous silica matrix. However, particle size and dispersion of the Co_3O_4 nanoparticles between the samples from the TEM images can be seen to be significantly different. The TEM image of CoES40 nanocomposite visually shows a narrow size distribution (5–10 nm) of which the Co_3O_4 nanoparticles are homogeneously dispersed throughout the silica network. Interestingly the Co_3O_4 nanoparticles formed almost fractal-like agglomerates of various shapes. In contrast, CoTEOS shows significantly larger Co_3O_4 nanoparticles, in the order of 20–60 nm, with well-demarcated shape, which are heterogeneously distributed.

Both XRD and TEM results are in good agreement with the EXFAS spectra of the CoTEOS and CoES40 samples as depicted in Fig. 3 whereby the CoTEOS had larger Co_3O_4 particle size but a lower concentration of Co_3O_4 phase than that of the CoES40 sample.

In Fig. 3a, k^2-weighted EXFAS spectra ($\chi(k)$) of the CoTEOS and CoES40 samples, as well as two reference compounds (i.e. CoO and Co_3O_4), are shown in Fig. 3. The amplitude of the oscillations of CoES40 sample was strongly reduced as compared with reference compounds and it did not match with either of them. Contrary to this, the oscillations of the CoTEOS sample were similar to those of Co_3O_4 and pronounced contributions were found at high *k* values, indicating a greater degree of order than the CoES40 sample, a dominant peak was found in the first shell, while it was weak in the second shell for the CoES40 sample in Fig. 3b, indicating a much better dispersion of Co_3O_4 nanoparticles in the silica matrix. Due to the lower degree of sintering of cobalt oxide in CoES40 sample, the amount of cobalt dispersion is greatly pronounced as evidenced in the TEM results. This has been previously suggested to be attributed to the rapid formation of cobalt (II) hydroxynitrates when catalyst activation takes place in the presence of nitrates at low temperatures [32,33]. On the other hand, the more prominent contributions from high radial distances were observed for the CoTEOS sample, which is in good agreement with conventional cobalt oxide silica materials [20].

3.3. Structural mechanistic study by in-situ SAXS

To gain insight into the effect of RTP temperature and metal oxides on the structural formation of the nanocomposites for the four different silica matrices (CoTEOS and CoES40 along with the corresponding pure silica gels), we carried out in-situ heating, synchrotron SAXS studies. As shown in Fig. 4, the background-subtracted SAXS scattering intensity, $I(q)$, of the nanocomposites are shown as a function of q value with increasing RTP temperature. For CoTEOS, before heating at 50 °C, the gel matrix showed a lack of X-ray scattering intensity due to a loosely-crosslinked, wet gel network containing a large amount of solvents (water and ethanol), and very small oligomeric particles. Hence, the level of scattering intensity is quite low and noisy. However, as the calcination temperature increased from 50 to 600 °C, CoTEOS displayed several structural transitions, which correlates well with increasing particles size of the spheres. Based on a spherical model, the average particle radius *R* increases from 0 to 28 Å, which means that at 50 °C the cobalt-containing gel particles are too small to be scattered. In

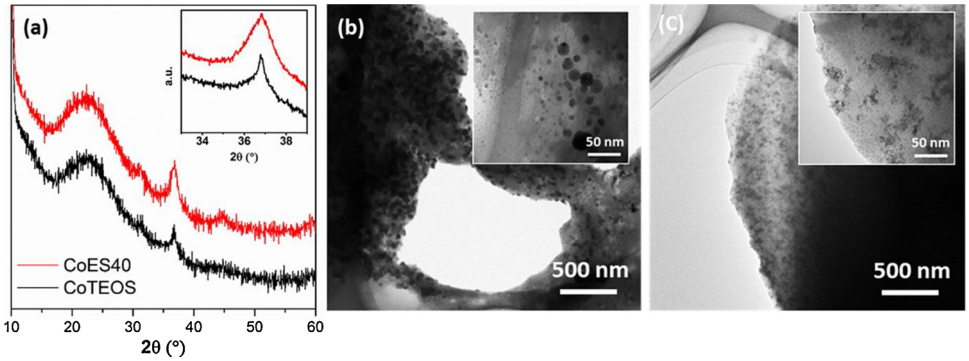

Fig. 2. (a) XRD pattern of Co_3O_4-silica catalysts with the inset image shows the focussed scans of the (311) reflection centred at 36.9° 2θ and TEM images of (b) CoTEOS and (c) CoES40 samples with the inset images showing the close-up of the respective figure.

comparison, these small gel particle population decreases rapidly as a function of calcination temperature, as observed by a decrease in the intensity at high q range. Another notable feature is marked by an increased population of the large spherical particles ca. 0.06 $Å^{-1}$, which corresponds to a particle radius R of 22–28 Å. This can be ascribed to the consolidation of primary building blocks of silica oligomers and hydrated cobalt ions into a condensed solid gel that consists of aggregated silica network and cobalt oxide as the solvent is removed during heating. Thus, both silica and cobalt oxide particle sizes grew at the expense of the primary silica polymeric particles and cobalt ions.

In contrast, CoES40 nanocomposite gel (Fig. 4b) exhibited a consistent scattering profile and intensity across the temperature range, albeit a small difference in intensity and slope is detected at low q range. For this series, the mass fractal model can be used to fit the branched polymeric structure, whereby the mass fractal provides an indication of the network compactness. Due to the similar intensity profile, it can be understood that CoES40 network is made up of monodisperse branched building blocks, which consolidate into highly branched agglomerates with only a slight loss in pore size and volume, which is indicated by the minor decrease in the fractal dimension from 2.9 to 2.3 with increasing temperature. This is in good agreement with the N_2 physisorption results (Fig. S2, ESI†). Therefore, the particle density and scattering intensity do not change significantly upon thermal consolidation. The relatively high backgrounds suggest a population of small particles (probably cobalt oxide) that are too small to properly resolve in these SAXS experiments. Unlike the CoTEOS sample though, these particles are stable over the entire temperature range and never transit into larger (R = 22–28 Å) particles. This suggests that the silica sol network and the cobalt (oxide) particles had retained almost the same size.

A parallel in-situ SAXS experiment involving the pure silica precursors (TEOS and ES40) sol-gel process and RTP treatment was conducted to further understand the effect of cobalt ions during RTP. Fig. 4 also shows the X-ray scattering profiles of the TEOS (Fig. 4c) and ES40 (Fig. 4d) with respect to the same RTP temperatures. First, the X-ray scattering of both TEOS-derived and ES40-derived gels irrespective of temperature show almost no change at low q range from 0.01 to 0.06 $Å^{-1}$ (TEOS) and 0.01 to 0.03 $Å^{-1}$ (ES40). After this point of inflection, the TEOS scattering intensity reached a minimum $I(q)$ and plateau contrasting with a continuous decrease of $I(q)$ for the ES40. With increasing temperature, this region shows subtle differences in both the profile and feature. The plateau in TEOS-derived gels is typically ascribed to an unchanged size for the small particles. Yet, this population decreases slightly during the heating, which can be seen by a small increasing shoulder peak between 0.015 and 0.03 $Å^{-1}$ as a result of silica aggregation and decreasing pore sizes from the thermal treatment, which is confirmed by. Such gel densification behaviour is typical of thermal condensation of silica gel above 200 °C.

On the other hand, ES40 gels produced increasing scattering at high q values between 0.03–0.3 $Å^{-1}$ with increasing temperature, which can be modelled as spheres with diameter ≤ 20 Å and probably correspond to the formation of the largest pores. This increasing scattering intensity

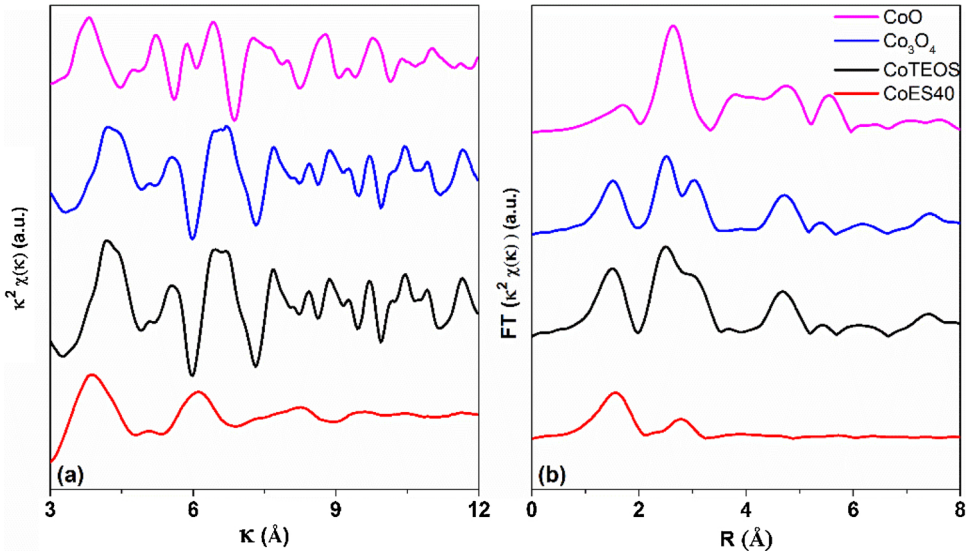

Fig. 3. Synchrotron x-ray absorption spectroscopy of (a) k^2 weighted $\chi(k)$ curves and (b) Fourier transforms of the Co K-edge of cobalt oxide silica samples and the CoO and Co_3O_4 reference compounds.

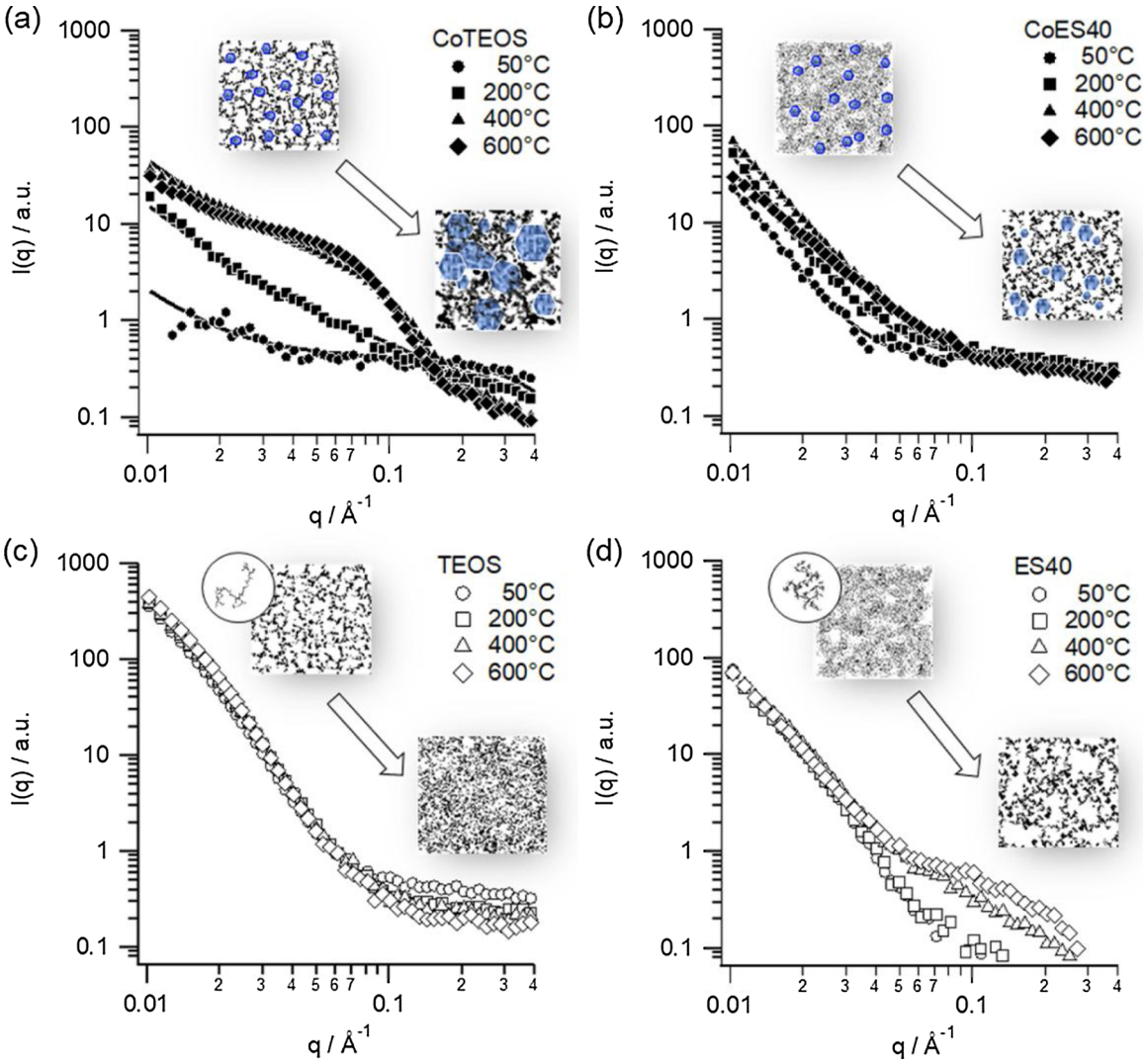

Fig. 4. Synchrotron in-situ SAXS patterns for (a) CoTEOS and (b) CoES40 nanocomposites with their fitting lines fit with a two-sphere plus mass fractal model ($R_{sphere1}$ = 5 Å plus $R_{sphere2}$ = 22–28 Å) and mass fractal model, respectively. Lines under data points are fits, uncertainties are within the size of the data points. For comparison, SAXS patterns for (c) TEOS- and (d) ES40-derived gels are provided.

indicates that the ES40 derived gels are producing larger pore wall thickness during the thermally-induced network consolidation above 200 °C. These cannot be observed in the CoES40 system because the scattering is dominated in this q range by small cobalt oxide particles. The rationale for this could also be inferred by an indifferent scattering profile of the ES40 silica gels at the low q range (0.03 Å^{-1}).

3.4. Fenton-like catalytic performance

Fenton-like catalysts show good organic pollutants degradation performance in aqueous solution and its activity can be significantly enhanced by the presence of cobalt ions [3,34]. The catalytic performance of both cobalt oxide silica nanocomposites and Co_3O_4 particles for the degradation of AO7 via an activated peroxymonocarbonate (APMC) was investigated and the UV–vis spectra of AO7 solution as a function of time. The oxidation of Co(II) ions in Co_3O_4-silica catalysts by peroxide (H_2O_2) in bicarbonate (HCO^{3-}) solution is expected to proceed via an activated peroxymonocarbonate (APMC) mechanism, in which free hydroxyl and carbonate radicals leads to the formation of other superoxide radicals such as perhydroxyl radical, superoxide ion, and singlet oxygen, which are all active for pollutant degradation under various conditions as shown in Eqs 1–8 [35,36].

$$Co_3O_4\text{-}Si + H_2O_2 \rightarrow {}^{\cdot}OH + HO^{\cdot} \quad (1)$$

$${}^{\cdot}OH + HCO_3^- \rightarrow H_2O + {}^{\cdot}CO_3^- \quad (2)$$

$${}^{\cdot}CO_3^- + H_2O_2 \rightarrow HCO_3^- + HO_2^{\cdot} \quad (3)$$

$$HO_2^{\cdot} \rightarrow H^+ + O_2^{\cdot -} \quad (4)$$

$$O_2^{\cdot -} + {}^{\cdot}OH \rightarrow O_2^1 + OH^- \quad (5)$$

$$HO_2^{\cdot} + O_2^{\cdot -} \rightarrow O_2^1 + HO_2^- \quad (6)$$

$$HO_2^{\cdot} + HO_2^{\cdot} \rightarrow O_2^1 + H_2O_2 \quad (7)$$

$$H_2O_2 + HCO_3^- \rightarrow H_2O + HCO_4^- \quad (8)$$

The APMC system has drawn significant attentions for the remediation of organic dye contamination from the textile industry due to its high oxidation efficiency under near-neutral or weakly alkaline conditions [35–37]. In this work, the APMC catalytic performance of both Co_3O_4-silica nanocomposites and the commercial Co_3O_4 particles for the degradation of AO7 was investigated and the UV–vis spectra of AO7 solution as a function of time during the tests is shown in Fig. 5. Both spectra show a major band at 484 nm, corresponding to the transition of the azo form [38], while the other two peaks at 230 and 310 nm at the ultraviolet region are attributed to the benzene and naphthalene rings

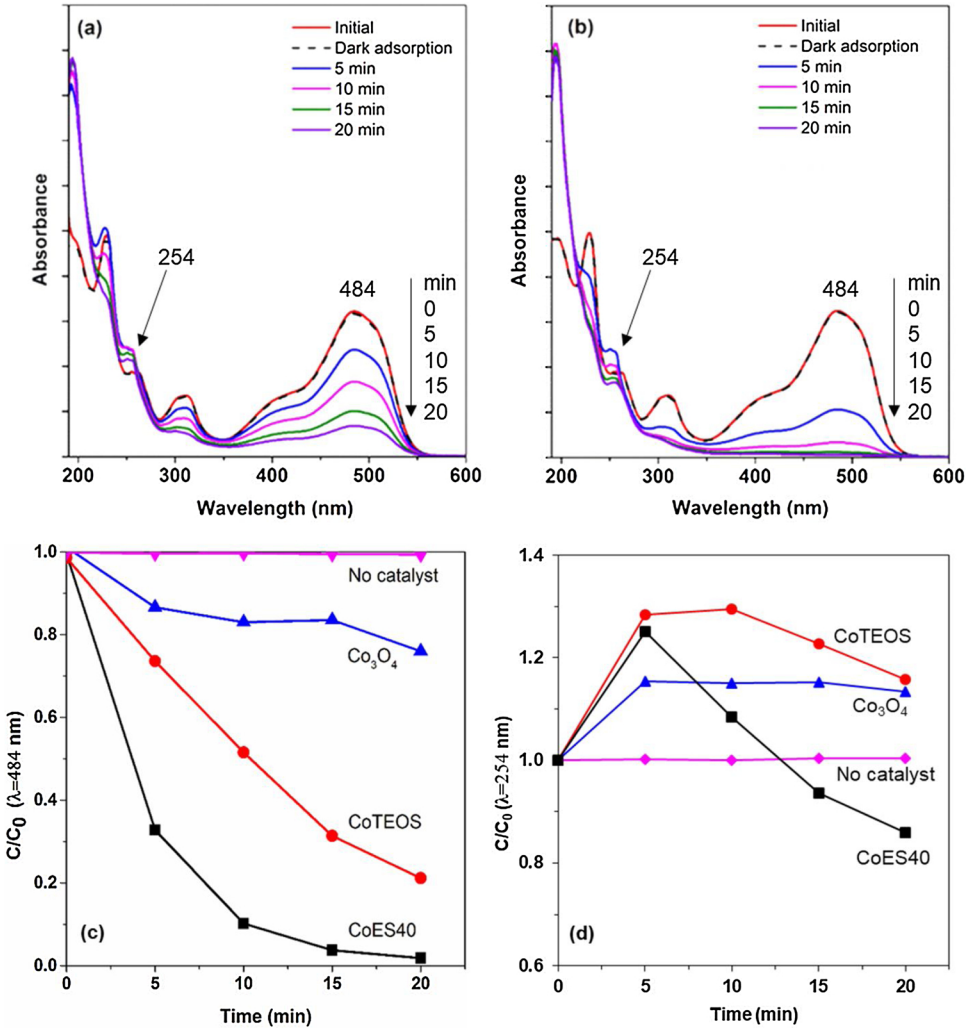

Fig. 5. UV–vis spectra of AO7 solution during degradation experiment by (a) CoTEOS and (b) CoES40 and the normalised peak intensity at (c) 484 nm and (d) 254 nm by the Co_3O_4-silica catalysts along with commercial Co_3O_4 catalyst.

of AO7 molecules [39]. The dark adsorption was negligible and reached equilibrium for both samples during the initial 30 min.

When H_2O_2 was added to initiate the reaction, it was clear that both solutions showed similar UV–vis patterns and all bands decreased with increasing of reaction time except for one band at 254 nm. Specifically, the reduction of the peak intensity at 484 nm confirmed the destruction of the chromophoric structure in the vicinity of the azo-linkage [40]. Meanwhile, the decrease of band intensities at 230 and 310 nm was due to the opening of the benzene and naphthalene ring. The peak intensity at 254 nm increased with time for the CoTEOS catalyst (Fig. 5a) and yet it showed an opposite trend for the CoES40 catalyst (Fig. 5b). This peak can be attributed to the presence of naphthalene type intermediates [28], which is expected to continue being generated from AO7 degradation and further degraded by the radicals.

The AO7 degradation profiles (484 nm) and the presence of naphthalene intermediates (254 nm) as a by-product in the reactor with Co_3O_4-silica catalysts or commercial Co_3O_4 catalyst are plotted in Fig. 5c and d, respectively. In the absence of the cobalt species (only HCO_3^- and H_2O_2), there was no degradation or the by-products observed in the first 20 min, which is in good agreement with other studies [3,37]. The commercial, pristine Co_3O_4 catalyst showed very slow AO7 degradation profile reaching to $C/C_0 = 0.76$ after 20 min (Fig. 5c). Similarly, in Fig. 5d, the C/C_0 intensity at 254 nm increased initially but levelled off after 5 min, which suggests that the naphthalene intermediates were also not being degraded. The degradation was remarkably improved when CoTEOS catalyst was used as a catalyst and the AO7 intensity was reduced to 0.21 after 20 min.. For the CoES40 catalyst, the AO7 intensity decreased to 0.1 and 0.02 at 10 min and 20 min, respectively, demonstrating a much faster kinetics than CoTEOS sample. This is also confirmed by the destruction of the naphthalene intermediates being much faster for the CoES40 at the outset in Fig. 5d.

To evaluate the catalyst reactivity of the samples, we used the Langmuir-Hinshelwood (L-H) model to interpret the AO7 degradation. If adsorption is relatively weak, the relationship of the concentration of the pollutant (C) and the apparent kinetic constant (k_{app}), can be expressed by a pseudo-first-order kinetic [41]:

$$\ln\left(\frac{C}{C_0}\right) = -k_r k_{ad}\, t = -k_{app} t$$

where k_r is the intrinsic rate constant and k_{ad} is the adsorption equilibrium constant. The k_{app} of CoES40 catalyst is 0.21 min^{-1} which is three-fold higher than that of the CoTEOS (k_{app} = 0.07 min^{-1}). In comparison, the samples treated by the CTP method yielded a k_{app} of 0.021 min^{-1} for CoTEOS and 0.027 min^{-1} for CoES40, which are ten-fold and three-fold lower than that of the corresponding RTP treated CoTEOS and CoES40 samples (see Fig. S3, ESI†). However, the kinetic rate constants determined in this study was still lower than that of the homogenous C_o^{2+} system, which is 0.50 min^{-1} for the reaction at AO7 concentration of 50 μM at 25 °C [42]. It is understandable as some

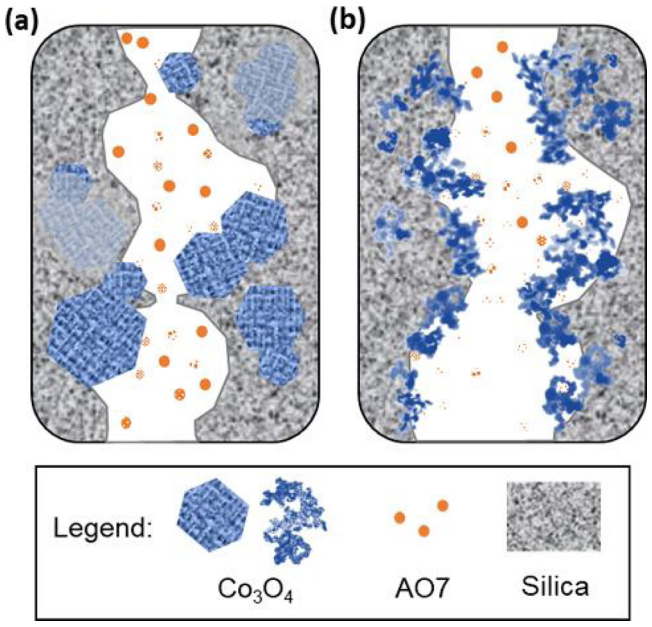

Fig. 6. Schematic structure of AO7 degradation by (a) CoTEOS and (b) CoES40.

cobalt species may not be accessible due to the presence of silica support in this work.

In order to understand the possibility of catalyst leaching and its contribution towards AO7 degradation, further degradation experiments were carried out using the leaching solution from the CoES40 catalyst (see ESI† for experimental procedure and results). By using ICP-AES, 0.60 ppm of leached cobalt concentration was detected after 1 h of soaking time. After the addition of AO7 to the leached solution, less than 25% of AO7 degradation was observed at the 20 min timepoint, while a near-complete degradation was achieved over the CoES40 catalyst. Considering the leaching solution also contained the radicals that had been formed by the CoSi during leaching process, the contribution of leached Co ions on AO7 degradation should be significantly lower.

Moreover, the high concentration of Co(III) could also be crucial. For homogenous Co^{2+}-HCO_3^--H_2O_2 system, it has been suggested that the bound hydroxyl radicals were the main reaction species during the oxidation of Co(II) to Co(III) by H_2O_2. The reduction of Co(III) was suggested to be the rate-limiting step, although it was not catalytically active [28]. The reduction of Co(III) in Co_3O_4 nanoparticles in our sample may provide more active $O_2^{-}\cdot$ radicals contributing to the degradation. However, the heterogeneous catalyst is more practical as it can reduce the risk of cobalt pollution. Furthermore, it is worth noting that the preparation time of the catalysts in this work was in less than 2 h, which equates to only 10% of material processing time compared to other Co_3O_4-silica catalysts derived by the conventional sol-gel and slow thermal processing method [43].

3.5. Proposed dye degradation mechanism

Sol-gel derived silica matrices are widely recognised to form percolative pathways which are composed of mesoporous regions interlinked with microporous constrictions or other mesoporous pockets [15]. The pore size tuning and a simple fabrication process make them ideal substrate material for catalysts [2,5,44], molecular sieves [1,45], and membrane reactors [46]. In this work, the superior catalytic performance CoES40 can be attributed to three aspects as shown in Fig. 6.

First, the pore size was slightly larger for CoES40 (Fig. S2, ESI†), thus the mass transfer within the nanocomposite matrix is expected to be larger. It may also offer easier access of the catalyst for the AO7 molecules, which has an estimated molecular size of 9.4 Å [47,48]. Secondly, cobalt phases in the CoES40 catalyst exhibited a much better dispersion and smaller sizes than those in the CoTEOS catalyst. Hence, more active catalytic sites could be expected in the CoES40 catalyst. It is worth noting that the CoES40 catalyst had a much higher concentration of Co(III), hence, also possibly accelerating the reduction rate.

4. Conclusions

Cobalt oxide silica nanomaterials were synthesised using a sol-gel method with two different silica precursors (i.e. TEOS and ES40) via a rapid thermal processing treatment. Cobalt oxide silica sample derived from TEOS produced a significantly lower concentration of Co_3O_4 than the sample derived from ES40. The majority of the cobalt phase in CoTEOS sample was Co(II), while it was mainly Co_3O_4 in CoES40, suggesting that the silica precursor played an important role in the formation of the cobalt phase. Moreover, X-ray spectroscopic results confirmed that the cobalt phase in CoES40 had a much better dispersion. The particle size of Co_3O_4 was measured to be 44 nm for CoTEOS while it was only 14 nm for CoES40, which agreed well with the TEM images. XAS results showed that cobalt in CoES40 had a very short-range order, indicating a high dispersity. When the materials were used for AO7 dye degradation with a HCO_3^-/H_2O_2 system, the CoES40 sample showed superior catalytic performance and the degradation efficiency was 98% after 20 min. The catalytic performance can be correlated to the well-dispersion of the cobalt phase and high concentration of Co(III). Moreover, the combination of sol-gel process and rapid thermal treatment provided an alternative way to the nanomaterial preparation, which can significantly reduce the fabrication time. Our findings here will not only guide the development of advanced catalyst materials with tailored structure and properties but also benefit the evolution of material processing techniques for reducing energy consumption as well as enhancing material processability and scalability to incorporate other interesting functionalities.

Declaration of Competing Interest

The authors declare that they have no known competing financial interests or personal relationships that could have appeared to influence the work reported in this paper.

Acknowledgments

D. K. Wang thanks the funding supports given by the Australian Research Council (DE150101687; DP190101734), and the Sydney Southeast Asia Centre. Z. A. M. Merican and D. K. Wang thank the funding support by Yayasan UTP for the Fundamental Research Grant (FRGS-YUTP). Part of this research was undertaken on the XAS beamline and SAXS/WAXS beamline at the Australian Synchrotron, Australia. The in-situ SAXS study was also supported by the Sydney Analytical Core Research Facilities. This work benefited from the use of the SasView application, originally developed under NSF Award DMR-0520547. SasView also contains code developed with funding from the EU Horizon 2020 programme under the SINE2020 project Grant No 654000.

Appendix A. Supplementary data

Supplementary material related to this article can be found, in the online version, at doi:https://doi.org/10.1016/j.apcatb.2019.118246.

References

[1] C. Yacou, S. Smart, J.C. Diniz da Costa, Long term performance cobalt oxide silica membrane module for high temperature H_2 separation, Energy Environ. Sci. 5 (2012) 5820–5832.

[2] F. Jiao, H. Frei, Nanostructured cobalt oxide clusters in mesoporous silica as efficient oxygen-evolving catalysts, Angew. Chem., Int. Ed. 48 (2009) 1841–1844.
[3] L. Zhou, W. Song, Z. Chen, G. Yin, Degradation of organic pollutants in wastewater by bicarbonate-activated hydrogen peroxide with a supported cobalt catalyst, Environ. Sci. Technol. 47 (2013) 3833–3839.
[4] B. Kamecki, J. Karczewski, T. Miruszewski, G. Jasiński, D. Szymczewska, P. Jasiński, S. Molin, Low temperature deposition of dense $MnCo_2O_4$ protective coatings for steel interconnects of solid oxide cells, J. Eur. Ceram. Soc. 38 (2018) 4576–4579.
[5] C.-Y. Liu, C.-F. Chen, J.-P. Leu, Tunable interconnectivity of mesostructured cobalt oxide materials for sensing applications, Sens. Actuators B Chem. 137 (2009) 700–703.
[6] J. Wan, W. Chen, C. Chen, Q. Peng, D. Wang, Y. Li, Facile synthesis of CoNi x nanoparticles embedded in nitrogen-carbon frameworks for highly efficient electrocatalytic oxygen evolution, Chem. Commun. 53 (2017) 12177–12180.
[7] X. Zhang, R. Liu, Y. Zang, G. Liu, G. Wang, Y. Zhang, H. Zhang, H. Zhao, Co/CoO nanoparticles immobilized on Co-N-doped carbon as trifunctional electrocatalysts for oxygen reduction, oxygen evolution and hydrogen evolution reactions, Chem. Commun. 52 (2016) 5946–5949.
[8] C. Zhu, D. Wen, S. Leubner, M. Oschatz, W. Liu, M. Holzschuh, F. Simon, S. Kaskel, A. Eychmüller, Nickel cobalt oxide hollow nanosponges as advanced electrocatalysts for the oxygen evolution reaction, Chem. Commun. 51 (2015) 7851–7854.
[9] A.Y. Khodakov, W. Chu, P. Fongarland, Advances in the development of novel cobalt Fischer-Tropsch catalysts for synthesis of long-chain hydrocarbons and clean fuels, Chem. Rev. 107 (2007) 1692–1744.
[10] X. Deng, H. Tüysüz, Cobalt-oxide-based materials as water oxidation catalyst: recent progress and challenges, ACS Catal. 4 (2014) 3701–3714.
[11] K. Asano, C. Ohnishi, S. Iwamoto, Y. Shioya, M. Inoue, Potassium-doped Co_3O_4 catalyst for direct decomposition of N_2O, Appl. Catal. B 78 (2008) 242–249.
[12] Y. Lou, L. Wang, Z. Zhao, Y. Zhang, Z. Zhang, G. Lu, Y. Guo, Y. Guo, Low-temperature CO oxidation over Co_3O_4-based catalysts: significant promoting effect of Bi_2O_3 on Co_3O_4 catalyst, Appl. Catal. B 146 (2014) 43–49.
[13] X. Chen, J. Chen, X. Qiao, D. Wang, X. Cai, Performance of nano-Co_3O_4 /peroxymonosulfate system: kinetics and mechanism study using Acid Orange 7 as a model compound, Appl. Catal. B 80 (2008) 116–121.
[14] T. Warang, N. Patel, R. Fernandes, N. Bazzanella, A. Miotello, Co_3O_4 nanoparticles assembled coatings synthesized by different techniques for photo-degradation of methylene blue dye, Appl. Catal. B 132-133 (2013) 204–211.
[15] Q. Lin, G. Yang, Q. Chen, R. Fan, Y. Yoneyama, H. Wan, N. Tsubaki, Design of a hierarchical meso/macroporous zeolite-supported cobalt catalyst for the enhanced direct synthesis of isoparaffins from syngas, ChemCatChem 7 (2015) 682–689.
[16] N.H. Chou, P.N. Ross, A.T. Bell, T.D. Tilley, Comparison of cobalt-based nanoparticles as electrocatalysts for water oxidation, ChemSusChem 4 (2011) 1566–1569.
[17] M. Elma, D.K. Wang, C. Yacou, J. Motuzas, J.C. Diniz da Costa, High performance interlayer-free mesoporous cobalt oxide silica membranes for desalination applications, Desalination 365 (2015) 308–315.
[18] L. Liu, D.K. Wang, D.L. Martens, S. Smart, E. Strounina, J.C. Diniz da Costa, Physicochemical characterisation and hydrothermal stability investigation of cobalt-incorporated silica xerogels, RSC Adv. 4 (2014) 18862–18870.
[19] L. Liu, D.K. Wang, D.L. Martens, S. Smart, J.C. Diniz da Costa, Influence of sol-gel conditioning on the cobalt phase and the hydrothermal stability of cobalt oxide silica membranesere, J. Membr. Sci. 475 (2015) 425–432.
[20] L. Liu, D.K. Wang, P. Kappen, D.L. Martens, S. Smart, J.C. Diniz da Costa, Hydrothermal stability investigation of micro- and mesoporous silica containing long-range ordered cobalt oxide clusters by XAS, Phys. Chem. Chem. Phys. 17 (2015) 19500–19506.
[21] M. Bittner, L. Helmich, F. Nietschke, B. Geppert, O. Oeckler, A. Feldhoff, Porous $Ca_3Co_4O_9$ with enhanced thermoelectric properties derived from Sol–Gel synthesis, J. Eur. Ceram. Soc. 37 (2017) 3909–3915.
[22] F. Kahraman, M.A. Madre, S. Rasekh, C. Salvador, P. Bosque, M.A. Torres, J.C. Diez, A. Sotelo, Enhancement of mechanical and thermoelectric properties of $Ca_3Co_4O_9$ by Ag addition, J. Eur. Ceram. Soc. 35 (2015) 3835–3841.
[23] D.K. Wang, J.C. Diniz da Costa, S. Smart, Development of rapid thermal processing of tubular cobalt oxide silica membranes for gas separations, J. Memb. Sci. 456 (2014) 192–201.
[24] K.V. Klementev, Extraction of the fine structure from x-ray absorption spectra, J. Phys. D Appl. Phys. 34 (2001) 209.
[25] M. Doucet, J.H. Cho, G. Alina, J. Bakker, W. Bouwman, P. Butler, K. Campbell, M. Gonzales, R. Heenan, A. Jackson, P. Juhas, S. King, P. Kienzle, J. Krzywon, A. Markvardsen, T. Nielsen, L. O'Driscoll, W. Potrzebowski, R. Ferraz Leal, T. Richter, P. Rozycko, T. Snow, A. Washington, SasView Version 4.1.2. Zenodo, 2017, https://doi.org/10.5281/zenodo.825675 August.
[26] A. Guinier, G. Fournet, Small-angle Scattering of X-rays, Wiley, New York, 1955.
[27] J. Teixeira, Small-angle scattering by fractal systems, J. Appl. Crystallogr. 21 (1988) 781–785.
[28] M. Luo, L. Lv, G. Deng, W. Yao, Y. Ruan, X. Li, A. Xu, The mechanism of bound hydroxyl radical formation and degradation pathway of Acid Orange II in Fenton-like Co^{2+}-HCO_3^- system, Appl. Catal. A Gen. 469 (2014) 198–205.
[29] N.S. Mcintyre, M.G. Cook, X-ray photoelectron studies on some oxides and hydroxides of cobalt, nickel, and copper, Anal. Chem. 47 (1975) 2208–2213.
[30] H. Xu, H.C. Zeng, Self-generation of tiered surfactant superstructures for one-pot synthesis of Co_3O_4 nanocubes and their close-and non-close-packed organizations, Langmuir 20 (2004) 9780–9790.
[31] M.C. Biesinger, B.P. Payne, A.P. Grosvenor, L.W.M. Lau, A.R. Gerson, R.S.C. Smart, Resolving surface chemical states in XPS analysis of first row transition metals, oxides and hydroxides: Cr, Mn, Fe, Co and Ni, Appl. Surf. Sci. 257 (2011) 2717–2730.
[32] J. Hong, E. Marceau, A.Y. Khodakov, A. Griboval-Constant, C. La Fontaine, V. Briois, A time-resolved in situ Quick-XAS investigation of thermal activation of Fischer–Tropsch silica-supported cobalt catalysts, Chem. Eur. J. 18 (2012) 2802–2805.
[33] J.R.A. Sietsma, J.D. Meeldijk, J.P. den Breejen, M. Versluijs-Helder, A.J. Van Dillen, P.E. de Jongh, K.P. de Jong, The preparation of supported NiO and Co_3O_4 nanoparticles by the nitric oxide controlled thermal decomposition of nitrates, Angew. Chem., Int. Ed. 46 (2007) 4547–4549.
[34] A. Xu, X. Li, S. Ye, G. Yin, Q. Zeng, Catalyzed oxidative degradation of methylene blue by in situ generated cobalt (II)-bicarbonate complexes with hydrogen peroxide, Appl. Catal. B 102 (2011) 37–43.
[35] E.V. Bakhmutova-Albert, H. Yao, D.E. Denevan, D.E. Richardson, Kinetics and mechanism of peroxymonocarbonate formation, Inorg. Chem. 49 (2010) 11287–11296.
[36] J.M. Lin, M. Liu, Chemiluminescence from the decomposition of peroxymonocarbonate catalyzed by gold nanoparticles, J. Phys. Chem. B 112 (2008) 7850–7855.
[37] X. Xu, D. Tang, J. Cai, B. Xi, Y. Zhang, L. Pi, X. Mao, Heterogeneous activation of peroxymonocarbonate by chalcopyrite (CuFeS 2) for efficient degradation of 2,4-dichlorophenol in simulated groundwater, Appl. Catal. B (2019) 273–282.
[38] E. Ember, S. Rothbart, R. Puchta, R. van Eldik, Metal ion-catalyzed oxidative degradation of Orange II by H_2O_2. High catalytic activity of simple manganese salts, New J. Chem. 33 (2009) 34–49.
[39] H. Park, W. Choi, Visible light and Fe (III)-mediated degradation of Acid Orange 7 in the absence of H_2O_2, J. Photochem. Photobiol. A: Chem. 159 (2003) 241–247.
[40] H. Chen, J. Motuzas, W. Martens, J.C. Diniz da Costa, Degradation of azo dye Orange II under dark ambient conditions by calcium strontium copper perovskite, Appl. Catal. B 221 (2018) 691–700.
[41] K. Kumar, K. Porkodi, F. Rocha, Langmuir–Hinshelwood kinetics–a theoretical study, Cataly. Commun. 9 (2008) 82–84.
[42] X. Long, Z. Yang, H. Wang, M. Chen, K. Peng, Q. Zeng, A. Xu, Selective degradation of orange ii with the cobalt(II)-bicarbonate-hydrogen peroxide system, Ind. Eng. Chem. Res. 51 (2012) 11998–12003.
[43] J.B. Silva, C.F. Diniz, R.M. Lago, N.D.S. Mohallem, Catalytic properties of nanocomposites based on cobalt ferrites dispersed in sol–gel silica, J. Non. Solids 348 (2004) 201–204.
[44] V. Musat, E. Fortunato, A.M.B. do Rego, R. Monteiro, Sol–gel cobalt oxide–silica nanocomposite thin films for gas sensing applications, Thin Solid Films 516 (2008) 1499–1502.
[45] L. Liu, D.K. Wang, D.L. Martens, S. Smart, J.C. Diniz da Costa, Binary gas mixture and hydrothermal stability investigation of cobalt silica membranes, J. Memb. Sci. 493 (2015) 470–477.
[46] S. Battersby, S. Smart, B. Ladewig, S. Liu, M.C. Duke, V. Rudolph, J.C. Diniz da Costa, Hydrothermal stability of cobalt silica membranes in a water gas shift membrane reactor, Sep. Purif. Technol. 66 (2009) 299–305.
[47] J.T. Edward, Molecular volumes and the Stokes-Einstein equation, J. Chem. Educ. 47 (1970) 261–270.
[48] H.P. Erickson, Size and shape of protein molecules at the nanometer level determined by sedimentation, gel filtration, and electron microscopy, Biol. Proc. Online 11 (2009) 32–51.